PHOTONICS Research

High-dimensional entanglement generation based on a Pancharatnam–Berry phase metasurface

Zhi-Xiang Li,[1,†] Dong Zhu,[1,†] Pei-Cheng Lin,[1] Peng-Cheng Huo,[1] Hong-Kuan Xia,[1] Ming-Ze Liu,[1] Ya-Ping Ruan,[1] Jiang-Shan Tang,[1] Miao Cai,[1] Hao-Dong Wu,[1] Chao-Ying Meng,[1] Han Zhang,[1] Peng Chen,[1] Ting Xu,[1] Ke-Yu Xia,[1,2,3,4] Li-Jian Zhang,[1,5] and Yan-Qing Lu[1,6]

[1]*National Laboratory of Solid State Microstructures, College of Engineering and Applied Sciences, and Collaborative Innovation Center of Advanced Microstructures, Nanjing University, Nanjing 210093, China*
[2]*Hefei National Laboratory, Hefei 230088, China*
[3]*Shishan Laboratory, Suzhou Campus of Nanjing University, Suzhou 215000, China*
[4]*e-mail: keyu.xia@nju.edu.cn*
[5]*e-mail: lijian.zhang@nju.edu.cn*
[6]*e-mail: yqlu@nju.edu.cn*

Received 19 July 2022; revised 8 September 2022; accepted 26 September 2022; posted 27 September 2022 (Doc. ID 470663); published 11 November 2022

High-dimensional entanglement is of great importance in quantum communications and can be realized by encoding information on multiple degrees of freedom (DoFs) of the photons. Conventionally, the realization of such high-dimensional entanglement involves different combinations of bulky optical elements. In this work, we present the use of a single dielectric metasurface to generate high-dimensional entanglement by modulating multi-DoFs of photons. By sending one of the polarization-entangled photons to interact with the metasurface, we encode path, spin angular momentum, and orbital angular momentum information to the original state. We achieve a four-qubit quantum state in the experiment. To verify it, we experimentally demonstrate the nonlocal correlations between the two photons by recording the correlated images, and we also perform a quantum state tomography measurement. This scheme can be applied to on-chip quantum state manipulation, which is promising in quantum communication with integrated components.

https://doi.org/10.1364/PRJ.470663

1. INTRODUCTION

Entanglement is at the heart of quantum technologies. The experimental preparation of entanglement states is a basic task in the field of quantum information. High-dimensional quantum entanglement has stronger nonlocality, larger information storage capacity, and better security performance [1–3]. The Hilbert space can be increased through the independent coding of different degrees of freedom (DoFs) of the photons, including path [4], frequency [5], and transverse-spatial modes [6–9]. Researchers have realized an equivalent of 20 qubits encoding in only two photons with two-qudit gates, taking advantage of the high dimensionality in two particular DoFs of a single photon—time and frequency [10]. Eighteen qubits encoded in three DoFs of six entangled photons have been demonstrated [11]. This is achieved by different combinations of bulky optical elements such as a beam displacer, polarization element, and spiral phase plate. With the development of high-performance compact and integrated optics [12], chip-scale generation of quantum entanglement is of great interest.

The metasurface has been suggested as a new platform for quantum optics. It offers the ability to enhance the functions and integration capabilities of quantum optical manipulations [13,14]. The metasurface is composed of nanoresonators with specially varying dimensions and orientations. It has enabled innovative flat-optics devices that often outperform the capabilities of bulk components [15–23]. Recently, metasurfaces have enabled multiphoton quantum state measurement and reconstruction [24], path encoded high-dimensional quantum source generation and multiphoton quantum sources [25], and spin angular momentum (SAM) and orbital angular momentum (OAM) entanglement of single photons [26]. Spatial entanglement and disentanglement of a two-photon state at a dielectric metasurface have been studied [27]. The concept of space-time quantum metasurfaces has been introduced [28]. The metasurface has also been used in the field of quantum edge detection [29]. Recent progress in dynamic control of quantum states using non-linear metasurfaces further enriches their functions [30]. These works have shown that the metasurface has great potential in quantum optical technologies.

However, the above-mentioned works mainly deal with one DoF or two DoFs of photons. It is reasonably expected to achieve high-dimensional entanglement through multiple DoF manipulation based on metasurfaces.

Here, taking advantage of the flexibility of a single dielectric metasurface, we show high-dimensional entanglement generation through joint modulation of the path, SAM, and OAM of photons. In our work, we send one of the entangled photons to interact with the metasurface for multi-dimensional information encoding. We experimentally demonstrate the nonlocal correlations between different DoFs by correlated imaging. We also measure the fidelity of the generated quantum state. Our results show that the metasurface can provide a novel integration platform for high-capacity optical communication applications.

2. METHODS AND RESULTS

The designed dielectric metasurface is a Pancharatnam–Berry (PB) phase-based fork-polarization grating (FPG) [27,31–33]. The PB phase is a geometric phase achieved by space-variant polarization manipulations. The FPG is essentially an inhomogeneous wave plate, like a combination of polarization gratings and a q-plate. Figure 1(a) shows the schematic diagram of the device. The metasurface is constructed from elliptic cylinders. Here the elliptic cylinders serve as wave plate elements, and the orientation of the fast axes depends on their spatial position. The function $\theta(x, y)$ describes the spatially variant distribution of the fast axes:

$$\theta(x, y) = \pi x/P + q\varphi, \tag{1}$$

where P is the period of the grating, and q is the charge value of the orientations with $\varphi = \arctan(y/x)$. This structure generates an extra geometric phase shift that is double the element's orientation angle:

$$\phi(x, y) = \pm(2\pi x/P + 2q\varphi), \tag{2}$$

where $m = 2q$ is the generated topological charge value of the FPG structure.

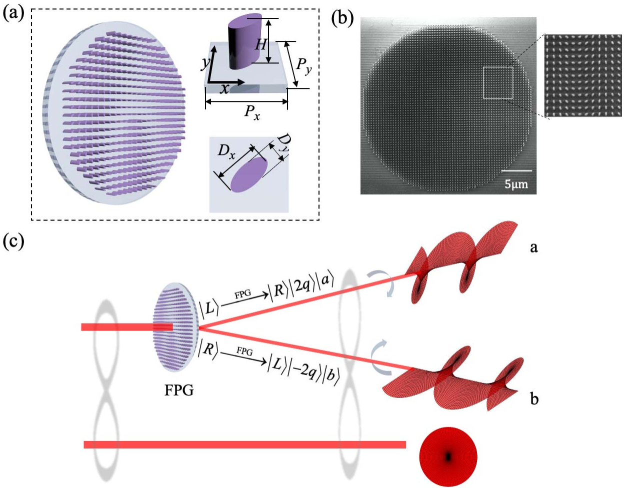

Fig. 1. (a) Schematic diagram of the proposed metasurface. The size of the spatially variant elliptic cylinders is $D_x = 210$ nm, $D_y = 100$ nm, and $H = 600$ nm. The periods are $P_x = P_y = 400$ nm. (b) Scanning electron micrograph (SEM) of the fabricated device. The metasurface was fabricated through a top-down nanofabrication process including e-beam lithography and inductively coupled plasma etching technology. (c) Schematic of the experimental concept.

This metasurface-based FPG can generate and control the propagation of the spin-polarized optical vortex with simultaneously coupled SAM-OAM-path modes. Gaussian mode photons pass through the FPG and diffract into three orders: ±1st-order OAM modes and zeroth-order Gaussian mode. The +1st- and −1st-order OAM modes have opposite topological charges and are always circularly polarized and orthogonal to each other. The zeroth-order photons are in a Gaussian mode with the same polarization as the input beam. If the input light is circularly polarized, it will diffract into the +1st/−1st order with orthogonal circular polarization. Thus, the FPG can simultaneously encode SAM, OAM, and path information into photons. Figure 1(b) shows a scanning electron micrograph of the metasurface. The diameter of the metasurface is 28 μm. The fabrication process is described in Appendix A. We design the FPG to deflect the incident light into two different output directions with angles of ±10°. We define the polarization conversion efficiency (PCE) as the ratio of the total energy of the left-handed (L) and right-handed (R) circularly polarized modes transmitted through the metasurface to the energy of the incident mode. The numerically simulated PCE of the designed FPG at 810 nm is 83.6%. The optical characterizations of the FPG metasurface are given in Appendix B.

In Fig. 1(c), we show the experimental scheme carried out by the device. The general idea is to start with two-photon polarization entanglement $\frac{1}{\sqrt{2}}(|R\rangle|R\rangle + |L\rangle|L\rangle)$. Then we send one photon to Alice and input the other photon (Bob's photon) to the meta-FPG device to encode OAM, SAM, and path information. We only consider the +1st and −1st diffraction orders of the device in our present work. This device performs the transformation $|R\rangle \overset{\text{FPG}}{\rightarrow} |L\rangle|-2q\rangle|b\rangle$ and $|L\rangle \overset{\text{FPG}}{\rightarrow} |R\rangle|2q\rangle|a\rangle$, where the left and right circular polarizations are converted to output states with opposite spin and $\pm 2q\hbar$ OAM in different optical paths. Hence, the created entangled biphoton state shared between Alice and Bob reads as follows:

$$\psi_{\text{FPG}} = \frac{1}{\sqrt{2}}(|L\rangle|-2q\rangle|b\rangle|R\rangle + |R\rangle|2q\rangle|a\rangle|L\rangle), \tag{3}$$

where q equals 0.5, and a and b represent the corresponding paths of the +1st and −1st diffraction orders. If we denote R, $2q$, a as logic 0, and L, $-2q$, b as logic 1, we arrive at a four-qubit high-dimensional state $\psi_{\text{FPG}} = \frac{1}{\sqrt{2}}(|1\rangle|1\rangle|1\rangle|0\rangle + |0\rangle|0\rangle|0\rangle|1\rangle)$.

In our experiment, polarization-entangled photons are generated via the spontaneous parametric downconversion process based on a Sagnac interferometer scheme [34]. We use a 10-mm-long PPKTP crystal (Raicol Crystals) with a grating period of 10 μm for frequency-degenerate type-II quasi-phase-matched collinear SPDC. The experimental setup to generate photon pairs is depicted in Fig. 2. We use a continuous-wave diode laser at 405 nm as the pump laser. The crystal is anti-reflection coated at 405 and 810 nm. The temperature of PPKTP is set at 27.8°C with the stability of ±0.1°C by a heating oven. The generated SPDC photon pairs are collimated by a lens with a focal length of 200 mm. For frequency and spatial

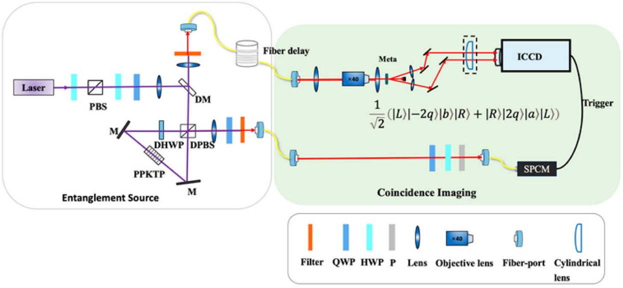

Fig. 2. Experimental setup to generate the entanglement and record the coincidence images. QWP, quarter-wave plate; HWP, half-wave plate; PBS, polarizing beam splitter; M, mirror; DM, dichroic mirror; DPBS, dual-wavelength PBS; DHWP, dual-wavelength HWP.

filtering, we implement a 3 nm bandpass filter and couple the generated photons into single-mode fibers. A half-wave plate set at 45° is inserted in one arm. We prepared the photon pairs in the state of $\frac{1}{\sqrt{2}}(|H\rangle|H\rangle - |V\rangle|V\rangle)$, which is equivalent to $\frac{1}{\sqrt{2}}(|R\rangle|R\rangle + |L\rangle|L\rangle)$. The average twofold coincidence count rate is about 90 kHz, measured with a 5 ns time window. We perform quantum state tomography to reconstruct the density matrix ρ of this state (Appendix C) [35]. The fidelity of an arbitrary quantum state ρ with respect to the desired pure state ρ_0 can be written as $F(\rho_0, \rho) = \mathrm{Tr}(\sqrt{\rho^{1/2}\rho_0\rho^{1/2}})$. According to our tomography result, the fidelity of this state is 93%.

The signal photons at Bob's side are focused on the device by a combination of lenses and an objective. After the photons pass through the FPG device, they are encoded with the path, SAM, and OAM information. The measured PCE is 40%. The relatively lower PCE is mainly due to the fabrication imperfection and the limited size of the device, as well as the imperfect alignments of the experimental setup. To directly verify the successful generation of the quantum state described in Eq. (1), we record the coincidence images by post-selection of different polarizations of the idler photon at Alice's [36–38].

The results are shown in Fig. 3. We use Alice's photon to trigger the intensified charge-coupled device (ICCD) for the detection of Bob's photons. In our experiment, a 35 m optical fiber delay line is used to compensate for the electric delay (70 ns) and the insertion delay of ICCD, ensuring that the signal photons reach the camera at the same time when the camera is triggered. We set the gate width of ICCD to 5 ns, and the images are obtained by summing over 60 images with an exposure time of 2 s. We chose the polarization of Alice's photon to be R and L separately, and then the ICCD recorded the path, OAM, and SAM information of Bob's photon. To examine the OAM topological charge of each diffracted beam, we recorded the photon distribution in the focal plane of a cylindrical lens. The number of the resulting tilted dark bands determines the absolute value of the topological charge, whereas the tilt direction gives its sign [39]. Besides, we verified the polarization states by using a polarization filter (PF). The PF is a combination of a quarter-wave plate (QWP) and a polarizer (not shown in the experiment setup), which allows only L to pass. We show the results in the right column in Fig. 3. When the trigger state of Alice's photons is R, Bob's photons with the polarization component L are recorded; while there is no obvious signal on the ICCD plane when the trigger state is L, indicating the polarization state of Bob's photons is R. Our results verify that the path, OAM, and SAM of Bob's photon are entangled with Alice's photon. The trigger-dependent images of the path, topological charge, and polarization information of Bob's photon are a direct observable signature of high-dimensional quantum entanglement.

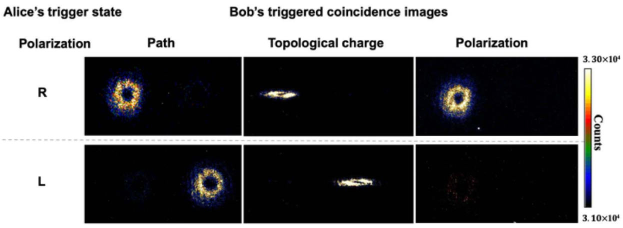

Fig. 3. Experimental results of the coincidence images. The first column tells Alice's trigger polarization with which the images are recorded. R and L represent right- and left-handed circular polarization. The images with the path, topological charge, and polarization information acquired at Bob's side depend on the trigger polarization. All images are given with a 99:1 contrast setting of the ICCD.

We also perform the quantum state tomography to further verify the entanglement. Here, instead of reconstructing a density matrix with 16 × 16 elements, we convert the generated state involving three DoFs of photons to a polarization entanglement state. We measured the fidelity of the resulting polarization entanglement. First, the two paths of the signal photons were combined interferometrically using a 27 mm long birefringent calcite beam displacer [40], after the beams passed through a quarter-wave plate (QWP). The function of the QWP is to transfer the R/L polarization state into the H/V polarization. The interference visibility was optimized with a suitable path compensation, and the measured maximum visibility reaches 93%. Note that if the path difference between H polarization and V polarization is longer than the coherence length, the state will lead to an entangled mixed state [41]. After the beam displacer, the path information has been projected into the polarization information. Then, we converted the OAM information into Gaussian mode by using another QWP and a q-plate. This QWP transfers linear polarizations to circular polarizations again, and the q-plate performs the transformation $|L\rangle|-2q\rangle \overset{q\text{-plate}}{\rightarrow} |R\rangle|0\rangle$ and $|R\rangle|2q\rangle \overset{q\text{-plate}}{\rightarrow} |L\rangle|0\rangle$. Finally, we coupled the Gaussian mode photons into a single-mode fiber for further analysis. The two-photon quantum state is now converted to the original polarization entanglement state. Figure 4(a) shows the quantum state tomography result, and Fig. 4(b) shows the experimental setup. According to the measured results, the fidelity of the reconstructed state is 82%. The reconstructed density matrix reflects the good quality of the high-dimensional entanglement state.

Overall, to verify the entanglement generated by the FPG metasurface, we conducted the coincidence imaging of high-dimensionally entangled quantum states and also performed the quantum tomography of these states. Our results show the nonlocal correlation and quantum entanglement of the generated photons. We only encode one of the entangled two photons here. If two metasurfaces are used separately to modulate Alice's and Bob's photons, one can easily obtain a six-qubit

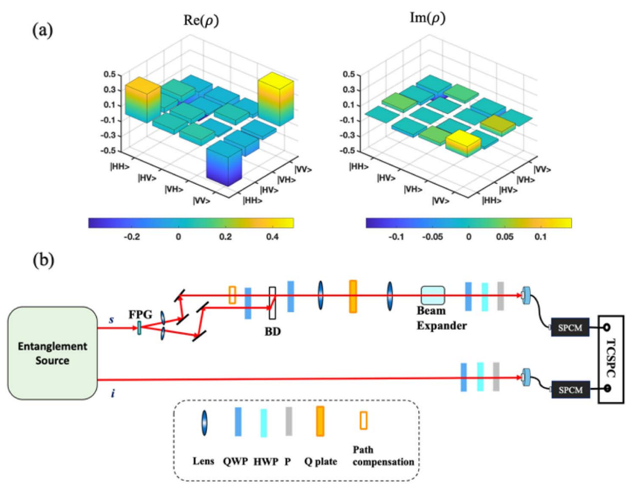

Fig. 4. (a) Real and imaginary parts of the reconstructed density matrix. (b) Experimental setup to perform the quantum state tomography.

quantum state $\frac{1}{\sqrt{2}}(|1\rangle^{\otimes 6} + |0\rangle^{\otimes 6})$. Moreover, with a different design of the metasurface, one can encode higher topological charges of the OAM mode or the number of the paths [31,42]; thus, various high-dimensional entanglement schemes can be achieved. Recent research reports multichannel distribution and transformation of entangled photons with two metasurfaces [43]. The function of the two metasurfaces in their work is to simultaneously distribute polarization-entangled photons to spatially separated multiple paths. Here, high-dimensional entanglement generation is achieved through the joint modulation of the path, SAM, and OAM of photons, which is associated with more DoFs and offers more flexibility.

3. CONCLUSION

In this work, we have developed a scheme for generating high-dimensional entanglement with an FPG metasurface. With the flexible light manipulation capability of the metasurface, we can encode path, OAM, and SAM information onto the entangled photons. This idea can be extended to generate and manipulate diverse entanglement states by using multifunctional metamaterials. Our work shows the feasibility of metasurfaces for the manipulations of different DoFs of quantum states. As the Hilbert space can be increased by expanding the dimensionality within each DoF of the photon, metasurfaces offer an excellent platform for high-dimensional quantum information processing. This scheme has the potential to achieve on-chip quantum state manipulation, which is promising in an overall integrated high-capacity quantum communication system [44,45].

APPENDIX A: FABRICATION OF THE FPG METASURFACE

The metasurface was fabricated through a top-down nanofabrication process including e-beam lithography (EBL) and inductively coupled plasma (ICP) etching technology. First, a 640 nm thick single-crystal silicon film on the sapphire substrate (SOS) was exposed to O_2 plasma to enhance adhesion. Then, a layer of 200 nm thick positive e-beam resist (ZEP520A) was spin-coated at 4000 r/min on the SOS substrate and baked on a hot plate for 3 min at 200°C. Subsequently, to reduce the charging effect during the EBL process, an E-spacer layer (ARPC5090) was spin-coated at 4000 r/min on the ZEP520A layer. An e-beam drawing system (TESCAN, MIRA3) at the acceleration voltage of 30 keV was used to expose the resist. The lateral profile of the metasurface was defined on the resist after development in ZED-N50. After that, a 30 nm thick Al layer as an etching hard mask was deposited on the structural resist by an e-beam evaporator (SKY, DZS500). Following a lift-off process in NMP, the patterns were transferred to the Al hard mask. Hereafter, the patterns were transferred to the 640 nm thick Si layer by an ICP etching system (Oxford, ICP180) using a mixture of C4F8 and SF6 chemistry. Finally, the expected sample was obtained after the removal of the residual Al mask with the mixture etching solution of phosphoric acid, acetic acid, and nitric acid.

APPENDIX B: OPTICAL CHARACTERIZATIONS OF THE FPG METASURFACE

In this section, we give the optical characterization of the FPG metasurface. To show the dependence of PCE on the

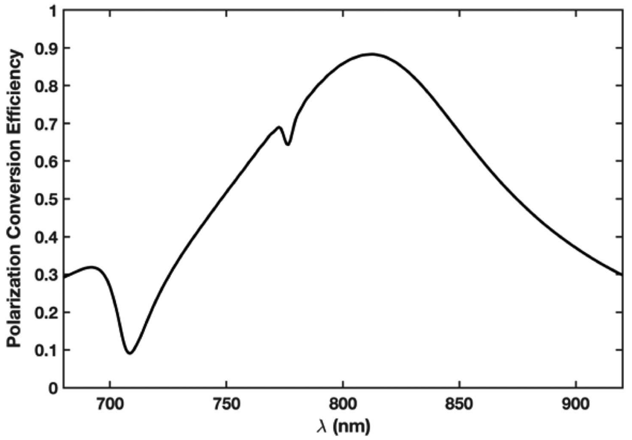

Fig. 5. Numerically simulated polarization conversion efficiency based on the wavelength.

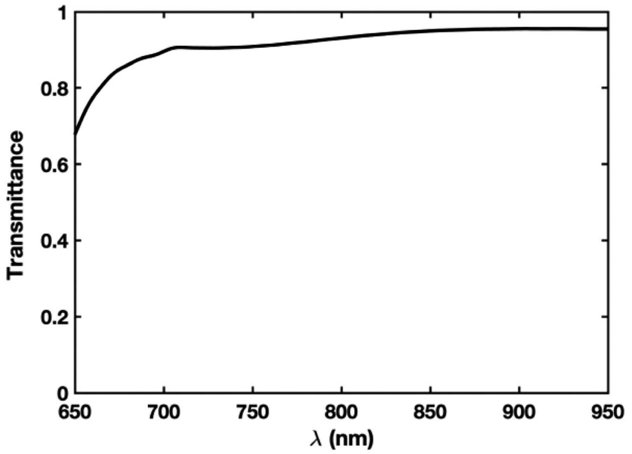

Fig. 6. Numerically simulated transmittance spectrum of the metasurface.

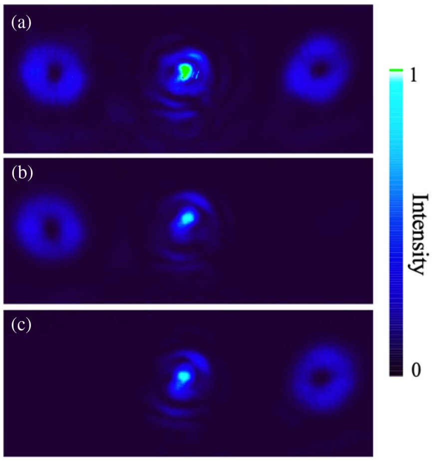

Fig. 7. Measured far-field diffraction intensity distributions of the metasurface. (a) Diffraction intensity distribution with a linearly polarized light incidence. (b) and (c) are the diffraction intensity distributions with R and L polarized incidence, separately. The results are obtained with a classical light source with a wavelength of 810 nm.

wavelength, we calculated the PCE curve, as shown in Fig. 5. The simulated PCE is above 50% during the wavelength range of 748–874 nm. Although our quantum experiments are conducted with photons at 810 nm, the device can work at a relatively broad wavelength range. In practice, by choosing suitable parameters of the structure, favorable efficiency at a targeting wavelength can be achieved.

Next, we calculated the transmittance spectrum of the designed metasurface. The result is given in Fig. 6. It exhibits the dependence of transmission on different wavelengths.

Experimentally, we measured the far-field intensity distributions of the metasurface. The results are obtained with a classical light source with a wavelength of 810 nm. Figure 7 shows the experimental results. Under an L-polarized incidence, 40% of the light will be deflected into the −1st diffraction order, which is consistent with measured PCE. This is mainly due to unavoidable factors, such as the finite size of the metasurface and fabrication imperfection, as well as imperfect experimental alignments. In our quantum experiments, as shown in the experimental setup in Fig. 2, only the photons in +1st and −1st diffraction orders are considered (the zeroth is being blocked); thus, this does not affect the quantum experimental results.

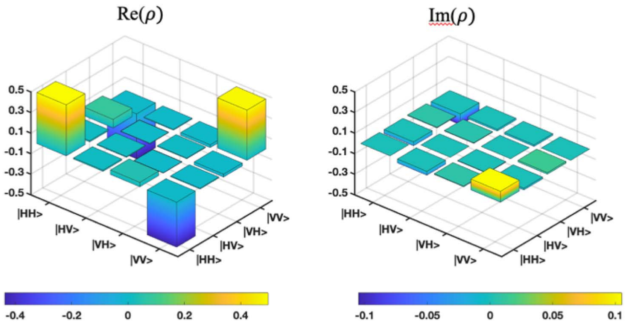

Fig. 8. Reconstructed density matrix of the original polarization entanglement state.

APPENDIX C: RECONSTRUCTED DENSITY MATRIX OF THE ORIGINAL ENTANGLEMENT STATE

The entanglement quality of the two-photon polarization state is quantified by quantum tomography and the reconstructed two-photon density matrix measurements [39]. The reconstructed density matrix is shown in Fig. 8.

Funding. National Key Research and Development Program of China (2017YFA0303700, 2019YFA0308700); Innovation Program for Quantum Science and Technology (2021ZD0301500, 2021ZD0301400); National Natural Science Foundation of China (11874212, 11890704, 61975077, 62175102, 62222507); Natural Science Foundation of Jiangsu Province (BK20212004); Program for Innovative Talents and Entrepreneurs in Jiangsu (JSSCTD202138).

Acknowledgment. We thank Prof. Jian-Ping Ding, Dr. Jian-Ji Liu, and Jin-Tao Pan for their helpful discussions.

Disclosures. The authors declare no conflicts of interest.

Data Availability. Data underlying the results presented in this paper are not publicly available at this time but may be obtained from the authors upon reasonable request.

[†]These authors contributed equally to this paper.

REFERENCES

1. M. Erhard, M. Krenn, and A. Zeilinger, "Advances in high-dimensional quantum entanglement," Nat. Rev. Phys. **2**, 365–381 (2020).
2. F. G. Deng, B. C. Ren, and X. H. Li, "Quantum hyperentanglement and its applications in quantum information processing," Sci. Bull. **62**, 46–68 (2017).
3. M. Malik, M. Erhard, M. Huber, M. Krenn, R. Fickler, and A. Zeilinger, "Multi-photon entanglement in high dimensions," Nat. Photonics **10**, 248–252 (2016).
4. X.-M. Hu, W.-B. Xing, B.-H. Liu, Y.-F. Huang, C.-F. Li, G.-C. Guo, P. Erker, and M. Huber, "Efficient generation of high-dimensional entanglement through multipath down-conversion," Phys. Rev. Lett. **125**, 090503 (2020).
5. Y. Chen, S. Ecker, L. Chen, F. Steinlechner, M. Huber, and R. Ursin, "Temporal distinguishability in Hong-Ou-Mandel interference for harnessing high-dimensional frequency entanglement," NPJ Quantum Inf. **7**, 167 (2021).
6. M. Hiekkamäki and R. Fickler, "High-dimensional two-photon interference effects in spatial modes," Phys. Rev. Lett. **126**, 123601 (2021).
7. M. Erhard, R. Fickler, M. Krenn, and A. Zeilinger, "Twisted photons: new quantum perspectives in high dimensions," Light Sci. Appl. **7**, 17146 (2018).
8. G. Molina-Terriza, J. P. Torres, and L. Torner, "Twisted photons," Nat. Phys. **3**, 305–310 (2007).
9. R. Qu, Y. Wang, M. An, F. Wang, Q. Quan, H. Li, H. Gao, F. Li, and P. Zhang, "Retrieving high-dimensional quantum steering from a noisy environment with *N* measurement settings," Phys. Rev. Lett. **128**, 240402 (2022).
10. P. Imany, J. A. Jaramillo-Villegas, M. S. Alshaykh, J. M. Lukens, O. D. Odele, A. J. Moore, D. E. Leaird, M. Qi, and A. M. Weiner, "High-dimensional optical quantum logic in large operational spaces," NPJ Quantum Inf. **5**, 59 (2019).
11. X.-L. Wang, Y.-H. Luo, H.-L. Huang, M.-C. Chen, Z.-E. Su, C. Liu, C. Chen, W. Li, Y.-Q. Fang, X. Jiang, J. Zhang, L. Li, N.-L. Liu, C.-Y. Lu,

and J.-W. Pan, “18-qubit entanglement with six photons’ three degrees of freedom,” Phys. Rev. Lett. **120**, 260502 (2018).

12. X. Chen, Z. Fu, Q. Gong, and J. Wang, “Quantum entanglement on photonic chips: a review,” Adv. Photon. **3**, 064002 (2021).
13. J. Liu, M. Shi, Z. Chen, S. Wang, Z. Wang, and S. Zhu, “Quantum photonics based on metasurfaces,” Opto-Electron. Advan. **4**, 200092 (2021).
14. A. S. Solntsev, G. S. Agarwal, and Y. S. Kivshar, “Metasurfaces for quantum photonics,” Nat. Photonics **15**, 327–336 (2021).
15. M. Liu, W. Zhu, P. Huo, L. Feng, M. Song, C. Zhang, L. Chen, H. J. Lezec, Y. Lu, A. Agrawal, and T. Xu, “Multifunctional metasurfaces enabled by simultaneous and independent control of phase and amplitude for orthogonal polarization states,” Light Sci. Appl. **10**, 107 (2021).
16. W. Pan, Z. Wang, Y. Chen, S. Li, X. Zheng, X. Tian, C. Chen, N. Xu, Q. He, L. Zhou, and S. Sun, “High-efficiency generation of far-field spin-polarized wavefronts via designer surface wave metasurfaces,” Nanophotonics **11**, 2025–2036 (2022).
17. J. Xiang, Z. Tao, X. Li, Y. Zhao, Y. He, X. Guo, and Y. Su, “Metamaterial-enabled arbitrary on-chip spatial mode manipulation,” Light Sci. Appl. **11**, 168 (2022).
18. P. Huo, M. Song, W. Zhu, C. Zhang, L. Chen, H. J. Lezec, Y. Lu, A. Agrawal, and T. Xu, “Photorealistic full-color nanopainting enabled by a low-loss metasurface,” Optica **7**, 1171–1172 (2020).
19. S. Wang, P. C. Wu, V.-C. Su, Y.-C. Lai, M.-K. Chen, H. Y. Kuo, B. H. Chen, Y. H. Chen, T.-T. Huang, J.-H. Wang, R.-M. Lin, C.-H. Kuan, T. Li, Z. Wang, S. Zhu, and D. P. Tsai, “A broadband achromatic metalens in the visible,” Nat. Nanotechnol. **13**, 227–232 (2018).
20. A. Vega, T. Pertsch, F. Setzpfandt, and A. A. Sukhorukov, “Metasurface-assisted quantum ghost discrimination of polarization objects,” Phys. Rev. Appl. **16**, 064032 (2021).
21. E. Tseng, S. Colburn, J. Whitehead, L. Huang, S.-H. Baek, A. Majumdar, and F. Heide, “Neural nano-optics for high-quality thin lens imaging,” Nat. Commun. **12**, 6493 (2021).
22. R. C. Devlin, A. Ambrosio, N. A. Rubin, J. P. B. Mueller, and F. Capasso, “Arbitrary spin-to–orbital angular momentum conversion of light,” Science **358**, 896–901 (2017).
23. F. Zhang, X. Xie, M. Pu, Y. Guo, X. Ma, X. Li, J. Luo, Q. He, H. Yu, and X. Luo, “Multistate switching of photonic angular momentum coupling in phase-change metadevices,” Adv. Mater. **32**, 1908194 (2020).
24. K. Wang, J. G. Titchener, S. S. Kruk, L. Xu, H.-P. Chung, M. Parry, I. I. Kravchenko, Y.-H. Chen, A. S. Solntsev, Y. S. Kivshar, D. N. Neshev, and A. A. Sukhorukov, “Quantum metasurface for multiphoton interference and state reconstruction,” Science **361**, 1104–1108 (2018).
25. L. Li, Z. Liu, X. Ren, S. Wang, V.-C. Su, M.-K. Chen, C. H. Chu, H. Y. Kuo, B. Liu, W. Zang, G. Guo, L. Zhang, Z. Wang, S. Zhu, and D. P. Tsai, “Metalens-array–based high-dimensional and multiphoton quantum source,” Science **368**, 1487–1490 (2020).
26. T. Stav, A. Faerman, E. Maguid, D. Oren, V. Kleiner, E. Hasman, and M. Segev, “Quantum entanglement of the spin and orbital angular momentum of photons using metamaterials,” Science **361**, 1101–1104 (2018).
27. P. Georgi, M. Massaro, K.-H. Luo, B. Sain, N. Montaut, H. Herrmann, T. Weiss, G. Li, C. Silberhorn, and T. Zentgraf, “Metasurface interferometry toward quantum sensors,” Light Sci. Appl. **8**, 70 (2019).
28. W. J. M. Kort-Kamp, A. K. Azad, and D. A. R. Dalvit, “Space-time quantum metasurfaces,” Phys. Rev. Lett. **127**, 043603 (2021).
29. J. Zhou, S. Liu, H. Qian, Y. Li, H. Luo, S. Wen, Z. Zhou, G. Guo, B. Shi, and Z. Liu, “Metasurface enabled quantum edge detection,” Sci. Adv. **6**, eabc4385 (2020).
30. D. Zhang, Y. Chen, S. Gong, W. Wu, W. Cai, M. Ren, X. Ren, S. Zhang, G. Guo, and J. Xu, “All-optical modulation of quantum states by nonlinear metasurface,” Light Sci. Appl. **11**, 58 (2022).
31. S. Chen, Y. Cai, G. Li, S. Zhang, and K. W. Cheah, “Geometric metasurface fork gratings for vortex-beam generation and manipulation,” Laser Photon. Rev. **10**, 322–326 (2016).
32. Y. Qiu, S. Tang, T. Cai, H. Xu, and F. Ding, “Fundamentals and applications of spin-decoupled Pancharatnam–Berry metasurfaces,” Front. Optoelectron. **14**, 134–147 (2021).
33. P. Chen, B.-Y. Wei, W. Ji, S.-J. Ge, W. Hu, F. Xu, V. Chigrinov, and Y.-Q. Lu, “Arbitrary and reconfigurable optical vortex generation: a high-efficiency technique using director-varying liquid crystal fork gratings,” Photon. Res. **3**, 133–139 (2015).
34. T. Kim, M. Fiorentino, and F. N. C. Wong, “Phase-stable source of polarization-entangled photons using a polarization Sagnac interferometer,” Phys. Rev. A **73**, 12316 (2006).
35. D. F. V. James, P. G. Kwiat, W. J. Munro, and A. G. White, “Measurement of qubits,” Phys. Rev. A **64**, 052312 (2001).
36. R. Fickler, G. Campbell, B. Buchler, P. K. Lam, and A. Zeilinger, “Quantum entanglement of angular momentum states with quantum numbers up to 10,010,” Proc. Natl. Acad. Sci. USA **113**, 13642–13647 (2016).
37. R. Fickler, M. Krenn, R. Lapkiewicz, S. Ramelow, and A. Zeilinger, “Real-time imaging of quantum entanglement,” Sci. Rep. **3**, 1914 (2013).
38. P.-A. Moreau, E. Toninelli, T. Gregory, R. S. Aspden, P. A. Morris, and M. J. Padgett, “Imaging Bell-type nonlocal behavior,” Sci. Adv. **5**, eaaw256 (2019).
39. M. W. Beijersbergen, L. Allen, H. E. L. O. van der Veen, and J. P. Woerdman, “Astigmatic laser mode converters and transfer of orbital angular momentum,” Opt. Commun. **96**, 123–132 (1993).
40. P. Xue, R. Zhang, H. Qin, X. Zhan, Z. H. Bian, J. Li, and B. C. Sanders, “Experimental quantum-walk revival with a time-dependent coin,” Phys. Rev. Lett. **114**, 140502 (2015).
41. N. A. Peters, J. B. Altepeter, D. Branning, E. R. Jeffrey, T.-C. Wei, and P. G. Kwiat, “Maximally entangled mixed states: creation and concentration,” Phys. Rev. Lett. **92**, 133601 (2004).
42. P. Liu, Y. Fu, X. Xie, C. Min, Y. Zhang, and X. Yuan, “High-efficiency monolayer metallic metasurface for modulation of orbital angular momentum,” Chin. Opt. Lett. **20**, 123601 (2022).
43. Y.-J. Gao, Z. Wang, Y. Jiang, R.-W. Peng, Z.-Y. Wang, D.-X. Qi, R.-H. Fan, W.-J. Tang, and M. Wang, “Multichannel distribution and transformation of entangled photons with dielectric metasurfaces,” Phys. Rev. Lett. **129**, 023601 (2022).
44. A. Orieux and E. Diamanti, “Recent advances on integrated quantum communications,” J. Opt. **18**, 083002 (2016).
45. Q. Wang, Y. Zheng, C. Zhai, X. Li, Q. Gong, and J. Wang, “Chip-based quantum communications,” J. Semicond. **42**, 091901 (2021).